



## Article

Fully exposed nickel clusters with electron-rich centers for high-performance electrocatalytic CO<sub>2</sub> reduction to COQi Hao<sup>a,b</sup>, Qi Tang<sup>a,c</sup>, Hai-Xia Zhong<sup>a,d</sup>, Jia-Zhi Wang<sup>a,c</sup>, Dong-Xue Liu<sup>b</sup>, Xin-Bo Zhang<sup>a,c,\*</sup><sup>a</sup> State Key Laboratory of Rare Earth Resource Utilization, Changchun Institute of Applied Chemistry, Chinese Academy of Sciences, Changchun 130022, China<sup>b</sup> Key Laboratory of Automobile Materials (Jilin University), Ministry of Education, School of Materials Science and Engineering, Jilin University, Changchun 130022, China<sup>c</sup> School of Applied Chemistry and Engineering, University of Science and Technology of China, Hefei 230026, China<sup>d</sup> Center for Advancing Electronics Dresden (CFAED) and Faculty of Chemistry and Food Chemistry, Technische Universität Dresden, Dresden 01062, Germany

## ARTICLE INFO

## Article history:

Received 28 March 2022

Received in revised form 17 April 2022

Accepted 1 June 2022

Available online 7 June 2022

## Keywords:

Sulfur regulation

Nickel clusters

Fully exposed metal sites

Carbon dioxide reduction reaction

Industrial current density

## ABSTRACT

Single-atom catalysts (SACs) have attracted increasing concerns in electrocatalysis because of their maximal metal atom utilization, distinctive electronic properties, and catalytic performance. However, the isolated single sites are disadvantageous for reactions that require simultaneously activating different reactants/intermediates. Fully exposed metal cluster catalyst (FECC), inheriting the merits of SACs and metallic nanoparticles, can synergistically adsorb and activate reactants/intermediates on their multi-atomic sites, demonstrating great promise in electrocatalytic reactions. Here a facile method to regulate the atomic dispersion of Ni species from cluster to single-atom scale for efficient CO<sub>2</sub> reduction was developed. The obtained Ni FECC exhibits high Faradaic efficiency of CO up to 99%, high CO partial current density of 347.2 mA cm<sup>-2</sup>, and robust durability under 20 h electrolysis. Theoretical calculations illuminate that the ensemble of multiple Ni atoms regulated by sulfur atoms accelerates the reaction kinetics and thus improves CO production.

© 2022 Science China Press. Published by Elsevier B.V. and Science China Press. All rights reserved.

## 1. Introduction

The electrocatalytic reduction reaction of carbon dioxide (CO<sub>2</sub>RR) to value-added chemicals and fuels associated with renewable energy sources opens up a promising way for tackling global warming issues and realizing carbon neutrality [1,2]. Aiming at achieving an efficient industrial CO<sub>2</sub>RR process, a robust catalyst is necessary to speed up CO<sub>2</sub> kinetics. It also allows the generation of a large current density at a low overpotential toward target products, while suppressing the unavoidable competing hydrogen evolution reaction (HER) in an aqueous system [3–5]. Over decades of investigations, the state-of-art Au and Ag catalysts have exhibited satisfying selectivity and activity for electrochemical CO<sub>2</sub> conversion to CO [6–9]. However, their complicated synthesis process, high cost, and questionable stability limit their large-scale application. To address these challenges, atomically dispersed earth-abundant transition metal atoms (e.g., Fe, Co, Ni, Zn, etc.) based catalysts have been developed as promising alternatives [10–14].

Fully exposed cluster catalyst (FECC) is a new type of atomically dispersed catalyst, which was first proposed by Ma et al. and applied to the thermal catalysis field [15]. Unlike conventional

metal clusters, all atoms in these clusters are in the coordination-unsaturated state. Besides, the absence of bulk-phase metal atoms allows metal atom exposure. These fully exposed metal atoms provide rich sites for the activation of reactants and intermediates, thereby giving FECC an unique superiority in the field of electrocatalysis. Recent studies have found that single-atom catalysts (SACs) have some inherent shortcomings such as the independent active centers, inevitable high onset potential, and insufficient activation/adsorption for reactants, which induce low energy efficiency and block their practical applications for industry [16,17].

The multi-atom catalytic center with neighboring metal atoms in the fully exposed metal cluster can regulate the adsorption and desorption of reactants and intermediates while achieving synergistic catalysis. In this way, the utilization of an FECC addresses the above issues by facilitating the fast adsorption and activation of reactants to enhance the catalytic performances via their multiple metal atoms [18,19]. Recent successes of atomically dispersed metal clusters support this point. For example, Jiao et al. [20] developed a novel catalyst that consists of Cu atom-pair anchored on Pd<sub>10</sub>Te<sub>3</sub> nanowires. The well-defined Cu<sup>0</sup>-Cu<sup>1+</sup> dual-atom structures promoted the CO<sub>2</sub> activation by adsorbing H<sub>2</sub>O and CO<sub>2</sub> on Cu<sup>1+</sup> and adjacent Cu<sup>0</sup> respectively, leading to a selective and efficient electrocatalytic reduction of CO<sub>2</sub> to CO. Furthermore, Su et al. [21] found that CuO clusters loaded on nitrogen-

\* Corresponding author.

E-mail address: [xbzhang@ciac.ac.cn](mailto:xbzhang@ciac.ac.cn) (X.-B. Zhang).

doped carbon can be converted to Cu<sub>2</sub>-CuN<sub>3</sub> clusters during electrocatalytic CO<sub>2</sub> reduction and that such *in-situ* generated atomic clusters can efficiently catalyze CO<sub>2</sub> to ethanol. The progresses inspired the development towards an FECC with definite and uniformly dispersed Ni clusters on carbon support which can effectively accelerate the CO<sub>2</sub> activation and enhance the interaction of intermediates, thus decreasing the onset potential toward efficient industrial CO<sub>2</sub>RR to CO.

This project worked on the fabrication of N, S co-coordinated Ni species anchored on carbon nanosheets (CNs) via a facile impregnation method, causing the controllable synthesis of Ni clusters to single-atoms on CNs via careful pyrolysis treatment from 700 to 1000 °C (NiNSC-700, NiNSC-800, NiNSC-900 and NiNSC-1000). Unexpectedly, NiNSC-900 demonstrates fully exposed and multiple adjacent metal centers, and exhibits excellent CO current density ( $j_{\text{CO}}$ ) of  $\sim 347 \text{ mA cm}^{-2}$  at  $-0.8 \text{ V}$  vs. reversible hydrogen electrode (RHE), which is adequate for the industrial electrolysis CO<sub>2</sub>RR process ( $250 \text{ mA cm}^{-2}$ ). Impressively, high selectivity of CO with Faradaic efficiency (FE<sub>CO</sub>) of 99% was reached at a low overpotential of 390 mV along with stable catalytic durability for 20 h electrolysis in  $0.5 \text{ mol L}^{-1}$  KOH electrolyte. Density functional theory (DFT) calculations affirm that the charge arrangement of multiple Ni centers regulated by the introduced S atoms can enhance the adsorption of \*COOH intermediates on Ni sites. The synergistic effect of these multiple Ni atoms sites reduces the energy barrier of CO<sub>2</sub>RR. This work therefore sheds light on the development of fully exposed metal cluster catalysts in promoting the electrocatalytic reaction.

## 2. Experimental

### 2.1. Materials

Potassium thiocyanate (MACKLIN, P816699, KSCN, 99.5%, metal basis), nickel acetate tetrahydrate (MACKLIN, N814837, NiC<sub>4</sub>H<sub>6</sub>O<sub>4</sub>·4H<sub>2</sub>O, 99.9%, metal basis), sodium citrate dihydrate (Aladdin, S116311, C<sub>6</sub>H<sub>5</sub>Na<sub>3</sub>O<sub>7</sub>·2H<sub>2</sub>O, 99%, AR), dicyandiamide (MACKLIN, D806321, C<sub>2</sub>H<sub>4</sub>N<sub>4</sub>, AR), potassium bicarbonate (Aladdin, P110485, KHCO<sub>3</sub>, 99.5%), potassium hydroxide (MACKLIN, P816404, KOH, 95%, GR), ethanol absolute (Sinoreagent, 10009228, C<sub>2</sub>H<sub>5</sub>OH, 99.7%, AR), sulfuric acid (Sinoreagent, 10021608, H<sub>2</sub>SO<sub>4</sub>, 95%–98%, GR), hydrochloric acid (Sinoreagent, 10011018, HCl, 36%–38%, AR), 5% Nafion solution (Dupont, D520), 212 Nafion membrane (Alfa Aesar), anion-exchange membrane (Fumasep, FAA-PK-130), high-purity argon and carbon dioxide (Changchun Juyang Gas Co., Ltd.,  $\geq 99.999\%$ ), carbon paper (Ce Tech Co. Ltd., N1S1007), gas diffusion layer (Sigracet, 39BB). The ultrapure water (resistivity,  $18.2 \text{ M}\Omega \text{ cm}$ ) was filtered from Milli-Q ultrapure water machine and used as the solvent for all the procedures. The chemicals were directly put into use, with none of the treatment or depuration.

### 2.2. Instrumentation

A micro-X Ray diffractometer acquired from Rigaku, which equipped with Cu K $\alpha$  ( $\lambda = 0.15406 \text{ nm}$ ), was implemented for collecting powder X-ray diffraction (XRD) patterns. The scanning electron microscopy (SEM) measurements were performed on a Hitachi S4800 field emission SEM equipment, which operates at a certain voltage of acceleration (10 kV). The transmission electron microscopy (TEM) techniques were carried out on a JEM-2100F TEM machine (operating voltage: 200 kV). The high-angle annular dark-field scanning transmission electron microscopy (HAADF-STEM) techniques were conducted on an FEI Titan Themis 60–300 instrument with a spherical aberration corrector working at

200 kV. The Raman spectra were collected by a micro-Raman spectrometer (Renishaw). The X-ray fine structures (XAFS) were performed on the beamline BL07A1 in NSRRC with the technical supports from Ceshigo Research Service (<https://www.ceshigo.com>). A Si (111) double-crystal monochromator was applied for monochromatizing the radiation. The X-ray absorption near-edge structures (XANES) and extended X-ray absorption fine structures (EXAFS) data processing and analysis were achieved by Athena software. N<sub>2</sub> adsorption/desorption isotherms were recorded on a Micromeritics ASAP 2020 adsorption analyzer. The X-ray photoelectron spectroscopy (XPS) measurements were carried out on a Thermo Scientific Nexsa instrument, wherein the spectra were standardized based on the C 1s binding energy at 284.4 eV. Electrochemical measurements were processed on a Biologic VMP3 electrochemical workstation at ambient conditions. <sup>1</sup>H nuclear magnetic resonance (NMR) spectra were recorded on Bruker NMR spectrometers (AVANCE-III HD 500). Gas components analysis was processed on a ThermoFisher Trace 1300 gas chromatography (GC) with the equipment of pulsed discharge detector (PDD) and flame ionization detector (FID).

### 2.3. Preparation of fully exposed nickel clusters

#### 2.3.1. Synthesis of the carbon nanosheets (CNs)

The CNs were synthesized via simple pyrolysis of sodium citrate [22]. Before pyrolysis, a certain amount of sodium citrate dihydrate was dried in an oven at the temperature of 150 °C for 40 h to remove the crystalline water. Then the dried powder was heated at a fixed temperature (800 °C) with a temperature rate ( $5 \text{ }^\circ\text{C min}^{-1}$ ) for 1 h under Ar atmosphere. The obtained black powder was dealt with  $5 \text{ mol L}^{-1}$  H<sub>2</sub>SO<sub>4</sub> aqueous solution for 12 h at the heating temperature of 90 °C, and processed through washing and vacuum filtering several times, before undergoing drying at 75 °C.

#### 2.3.2. Synthesis of NiNSC-700 to NiNSC-1000

Nickel acetate tetrahydrate (8.5 mg) and KSCN (6.7 mg) were dissolved in a mixed solution of ultrapure water (1 mL) and ethanol absolute (1 mL) under continuous stirring for 1 h. Then 100 mg of CNs were added, and the slurry was mixed well by stirring for another 12 h. The evenly distributed slurry was heated at 75 °C for 12 h and ground into black power. The black power and 500 mg of dicyandiamide were separately placed at each side of the porcelain boat and heated under Ar flow condition, wherein the pyrolysis temperatures were set as 700–1000 °C separately to synthesize NiNSC-700 to NiNSC-1000. After acid leaching processes in  $3 \text{ mol L}^{-1}$  HCl, the samples were harvested by centrifugation with ultrapure water and alcohol several times, as well as drying at 75 °C overnight.

#### 2.3.3. Synthesis of N, S Ni NPs

N, S Ni NPs were synthesized using a similar process to NiNSC-900 fabrication. With the replacement of pyrolysis atmosphere (Ar) with 5% H<sub>2</sub>/Ar and the removal of acid leaching step.

#### 2.3.4. Electrode preparation

The catalyst (10 mg) was dispersed in a mixed solution of ethanol (400  $\mu\text{L}$ ) and Nafion solution (100  $\mu\text{L}$ ) by continuous sonication for 1 h. The dispersion liquid was drop-casted on a carbon paper for H-type cell (catalyst weight,  $0.5 \text{ mg cm}^{-2}$ ; reaction area,  $1 \text{ cm}^2$ ) and gas diffusion layer flow cell tests (catalyst weight,  $1 \text{ mg cm}^{-2}$ ; reaction area,  $1.1 \text{ cm}^2$ ), respectively. The geometric surface area was adjusted for calculating the current density.

## 2.4. Electrochemical measurements

The appraisals of electrocatalytic CO<sub>2</sub>RR performance were carried out in a classical three-electrode H-type cell and homemade flow cell system, separately. Ag/AgCl electrode with saturated KCl was adopted as the reference electrode. Pt mesh and Ni foil were applied as the counter electrode for H-cell and flow cell, respectively. The linear sweep voltammetry (LSV) curves were acquired with scan rate of 10 mV s<sup>-1</sup>. An AC voltage and amplitude voltage of 10 mV were applied to perform the electrochemical impedance spectroscopy (EIS) techniques, in which the frequency was set from 100 kHz to 0.1 Hz. The electrochemical active surface area (ECSA) of the samples were quantified by C<sub>dl</sub> obtained from cyclic voltammetry curves under a potential range of 0.2–0.3 V vs. RHE, a scanning speed of 2–14 mV s<sup>-1</sup>, and an interval of 2 mV s<sup>-1</sup>. The chronoamperometry (CA) tests were conducted at various potentials for 20 min, wherein online GC was applied for detecting the gaseous products. All potentials were switched to reversible hydrogen electrodes, which could be calculated by the equation [23]:

$$E(\text{vs. RHE}) = E(\text{vs. Ag/AgCl}) + 0.05916 \text{ pH} + 0.197. \quad (1)$$

The Faradic efficiency (FE) of the product was calculated by the equation [23]:

$$FE = \frac{Q_{\text{CO}}}{Q_{\text{total}}} = \frac{Z \times n \times F}{Q_{\text{total}}}, \quad (2)$$

where,  $Q$  is the quantity of electric charge through the reaction;  $Z$  is the number of transferred electrons, which is 2 for CO and H<sub>2</sub>;  $n$  is the mole number for a certain product;  $F$  is Faraday constant, 96,485 C mol<sup>-1</sup>.

## 2.5. Computational details

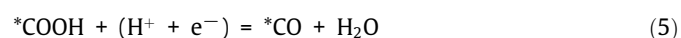
The supplied DFT calculations driven by first-principles theory were computed with Vienna *Ab Initio* Simulation Package (VASP) [24], which is equipped with the method of “Projector Augmented Wave” (PAW) [25]. The exchange-functional was managed by “Generalized Gradient Approximation” (GGA) of “Perdew–Burke–Ernzerhof” (PBE) functional [26]. The Spin-polarizations were utilised for all calculations. The plane wave’s energy cutoff was less than 0.03 eV Å<sup>-1</sup>, which originated from the expansion and force on each atom, in line with the convergence rule of geometric relaxation. The  $k$ -points in the Brillouin zone were sampled by a 2 × 2 × 1 grid. The self-consistent calculations employ a certain threshold for convergence energy (10<sup>-5</sup> eV). The DFT-D3 method was employed for evaluating the van der Waals interaction [27]. The computational models were established based on a 6 × 7 supercell with single-layer graphene (001) surface, which contains 84 atoms. A vacuum of 15 Å was adopted along the  $z$ -axis to prevent interactions of cyclical constructions.

The free energies of the CO<sub>2</sub> reduction process were obtained via the equation [28]:

$$\Delta G = \Delta E_{\text{DFT}} + \Delta E_{\text{ZPE}} - T\Delta S, \quad (3)$$

where  $\Delta E_{\text{DFT}}$  is the difference of each step’s DFT electronic energy;  $\Delta E_{\text{ZPE}}$  is the zero-point energy correction;  $\Delta S$  is the change in entropy. The above parameters were acquired by analyzing the vibration.  $T$  is temperature, 300 K in this instance.

The following equations are described for the reaction of CO<sub>2</sub> to CO:



where  $*$  is the active site on the catalytic surface.

## 3. Results and discussion

The schematic showing the synthesis of Ni FECC is demonstrated in Fig. 1a. Herein, KSCN acts as a strong chelating agent for coordination with Ni<sup>2+</sup>, and the formed Ni-SCN chelates will be absorbed on the surface of CNs substrates by the functional groups and defects using the wet chemistry method [29]. The excellent chelating effect brings about a dense spatial distribution of Ni atoms and results in the formation of multiple atom centers during the pyrolysis process at different temperatures. The XRD patterns of CNs and Ni FECCs are shown in Fig. S1a (online), in which the broad graphite peaks of Ni FECCs located at 24.1° and 44.1° are similar with CNs, confirming the amorphous states of Ni species and excluding the presence of crystalline Ni nanoparticles [17]. For comparison, Ni nanoparticles embedded N, S co-doped CNs (N, S Ni NPs) were also synthesized by pyrolyzing the precursors under Ar/H<sub>2</sub> atmosphere to explore the size effect. The XRD pattern of N, S NiNPs in Fig. S1b (online) exhibits three peaks located at 44.5°, 51.8°, and 76.4°, respectively, which attribute to the (1 1 1), (2 0 0), and (2 2 0) crystalline surfaces of metallic Ni [23]. The SEM images of Ni FECCs and N, S Ni NPs (Fig. S2 online) exhibit similar stacked and crosslinked nanosheets’ morphologies with CNs due to the excellent thermal stability of carbon matrix under high-temperature conditions. The TEM images of N, S Ni NPs (Figs. S3 and S4 online) demonstrate that Ni nanoparticles with diameters of approximately 50 nm were deposited on the CN substrates, accompanied with exposed (1 1 1) plane, which is consist with the XRD pattern of N, S Ni NPs. On the contrary, Ni nanoparticles were not observed for Ni FECCs, attributing to the elimination of crystalline Ni species by the acid leaching processes (Figs. S5–S8 online) [30]. Their annular patterns in selected area electron diffraction (SAED) images further suggest the absence of crystalline phase. The HAADF-STEM measurements were carried out to accurately verify the dispersion of Ni species, and numerous bright dots on the CNs were observed in Fig. 1b–e, which are ascribed to Ni atoms. Since the dispersity of the atomic Ni species on CN increases with increasing of pyrolysis temperature, a lack of crystalline phase of Ni clusters indicates the successful construction of fully exposed cluster sites. Notably, abundant well-organized adjacent atoms were detected in NiNSC-900 (Fig. 1d and Fig. S12 online), originating from the formation of dual-atom and ternary-atom cluster sites [31]. Conversely, a majority of isolated dots that belong to single Ni atoms were observed in NiNSC-1000 (Fig. 1e and Fig. S13 online). The relevant energy-dispersive X-ray spectroscopy (EDS) images disclose the homogeneous distribution of Ni, N, and S elements on Ni FECC samples (Fig. 1g–j, and Figs. S10, S11, and S13 online). The corresponding Ni loadings are 0.35 wt% for NiNSC-700, 0.29 wt% for NiNSC-800, 0.27 wt% for NiNSC-900, 0.20 wt% for NiNSC-1000, and 1.66 wt% for N, S Ni NPs respectively, as detected by inductively coupled plasma optical emission spectrometry detection (ICP-OES, Table S1 online). Despite the preserved morphology of CNs, abundant defects were induced by doping S and N under the pyrolysis process as indicated by the higher ratio of I<sub>D</sub>/I<sub>G</sub> (D, disorder band; G, graphite band) in the Raman spectra of NiNSC samples (Fig. S14 online). Among Ni FECC samples, NiNSC-900 exhibits a maximum ratio of I<sub>D</sub>/I<sub>G</sub>, associated with its higher density of defects [32]. When the heating temperature was raised to 1000 °C, NiNSC-1000 exhibited a decreased ratio of I<sub>D</sub>/I<sub>G</sub> and thus a higher graphitization degree.

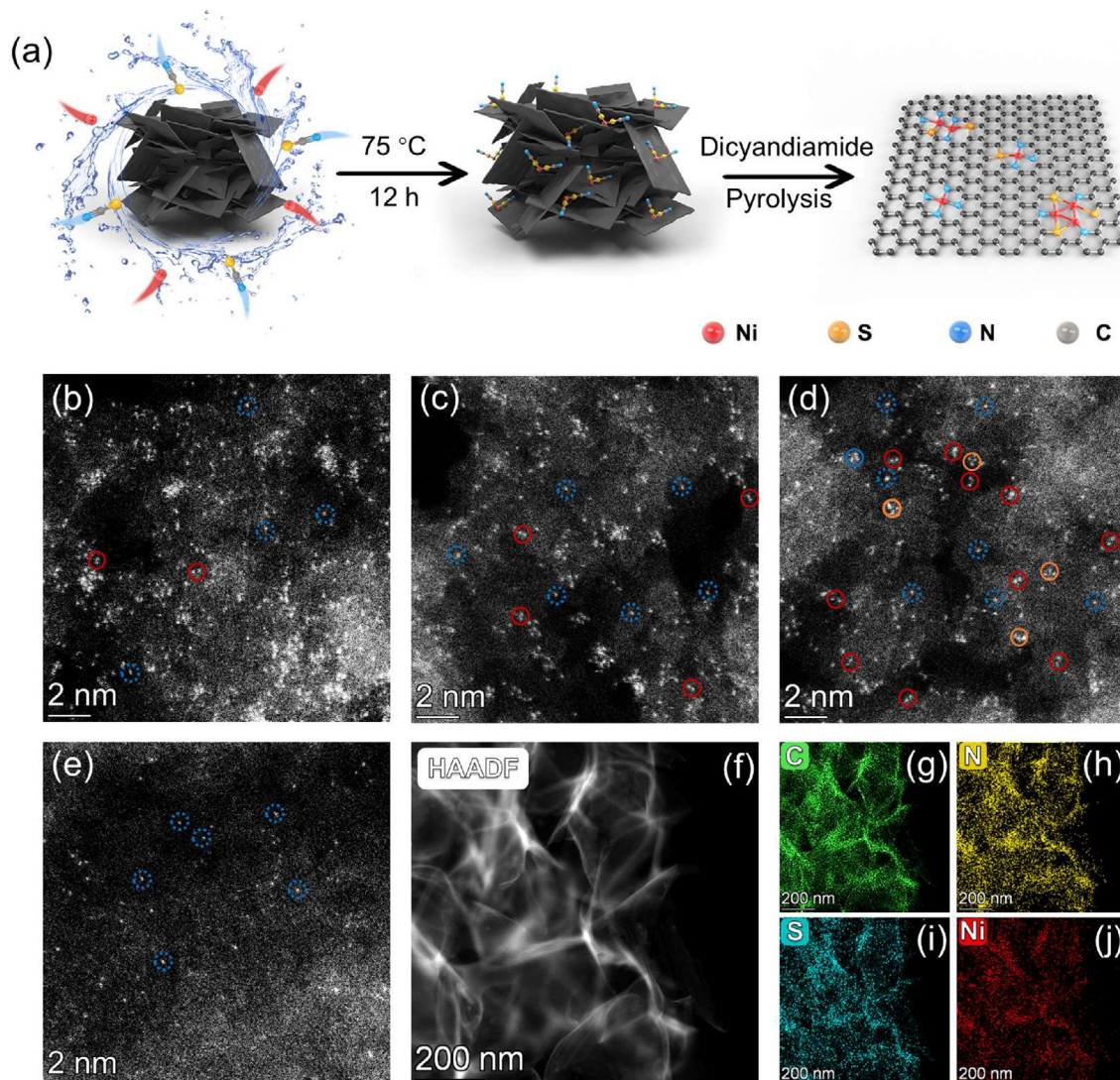


**Fig. 1.** (a) Schematic synthesis procedure of Ni FECC. (b–e) High-resolution HAADF-STEM images of NiNSC-700 (b), NiNSC-800 (c), NiNSC-900 (d) and NiNSC-1000 (e). (f–j) Low-resolution HAADF-STEM and corresponding EDS mapping of NiNSC-900.

To investigate the specific surface area, pore structure and volume, nitrogen adsorption and desorption isotherms were acquired at 77.3 K (Fig. S15a–e online). NiNSC-900 has the highest Brunauer-Emmett-Teller (BET) surface area of  $194.950 \text{ m}^2 \text{ g}^{-1}$  among the synthesized samples (Table S2 online), which is favorable for sufficient gas diffusion and exposure of more active sites [33]. Due to the stability of the carbon skeleton during the pyrolysis procedure, only a negligible reduction of pore volume was found in NiNSC samples. Moreover, NiNSC-900 possesses the highest  $\text{CO}_2$  adsorption capacity among the catalysts at  $25.17 \text{ cm}^3 \text{ g}^{-1}$ , which is 4.5 fold higher than that of N, S Ni NPs (Fig. S15f online). Thus, NiNSC-900, featured with more recognizable and accessible sites, has advantages in adsorbing and activating  $\text{CO}_2$  molecules [32].

To reveal the fine structures and chemical states of multiple Ni atom sites, XAFS and XPS techniques were implemented. The XANES and EXAFS spectra are shown in Fig. 2a–c. The near edges of Ni FECCs locate between those of Ni foil and NiO/NiS, demonstrating the oxidation states of Ni are between 0 and +2 [23,30]. In addition, the near edges of Ni FECCs exhibit a positive shift tendency upon increasing the heating temperature, consisting with the positive shift of the binding energy of Ni 2p orbits based on

the XPS analysis (Fig. 2d). This suggests the decrease of metallic states of Ni species from clusters to single-atoms [34]. The coordination environments of Ni species were identified by EXAFS measurements, and the radial distribution function curves for EXAFS spectra are displayed in Fig. 2b. The main peak at  $\sim 2.18 \text{ \AA}$  is ascribed to the Ni–Ni bond on the first shell for Ni foil. The prominent peak ascribed to the Ni–O–Ni bond corresponds at  $\sim 2.67 \text{ \AA}$  for NiO. And the maximum intensity of nickel phthalocyanine (NiPc) at  $\sim 1.50 \text{ \AA}$  can be identified as a Ni–N bonding. For NiS, the peak at  $\sim 1.92 \text{ \AA}$  is regarded as Ni–S bonding [35]. The first peak at  $\sim 1.38 \text{ \AA}$  for NiNSC-900 is attributed to the Ni–N bonding, and the peaks at  $\sim 1.96$  and  $2.39 \text{ \AA}$  originate from Ni–S and Ni–Ni bonding, respectively. Furthermore, similar Ni–N and Ni–S shell peaks with NiNSC-900 are shared by NiNSC-700 and NiNSC-800. For NiNSC-1000, only one peak attributes to Ni–N, which could be observed at  $\sim 1.26 \text{ \AA}$  with the absence of overlapping peaks, in line with the HAADF-STEM measurements and the single-site dispersed Ni species in NiNSC-1000 [36]. The detailed coordination number (CN) and fitted EXAFS plots of the above samples were acquired as the basis of atomic modeling (Fig. 2c, Fig. S16 and Table S3 online). The high-resolution N 1s and S 2p XPS spectra of Ni FECCs are shown in Fig. S17 (online), indicating the presence

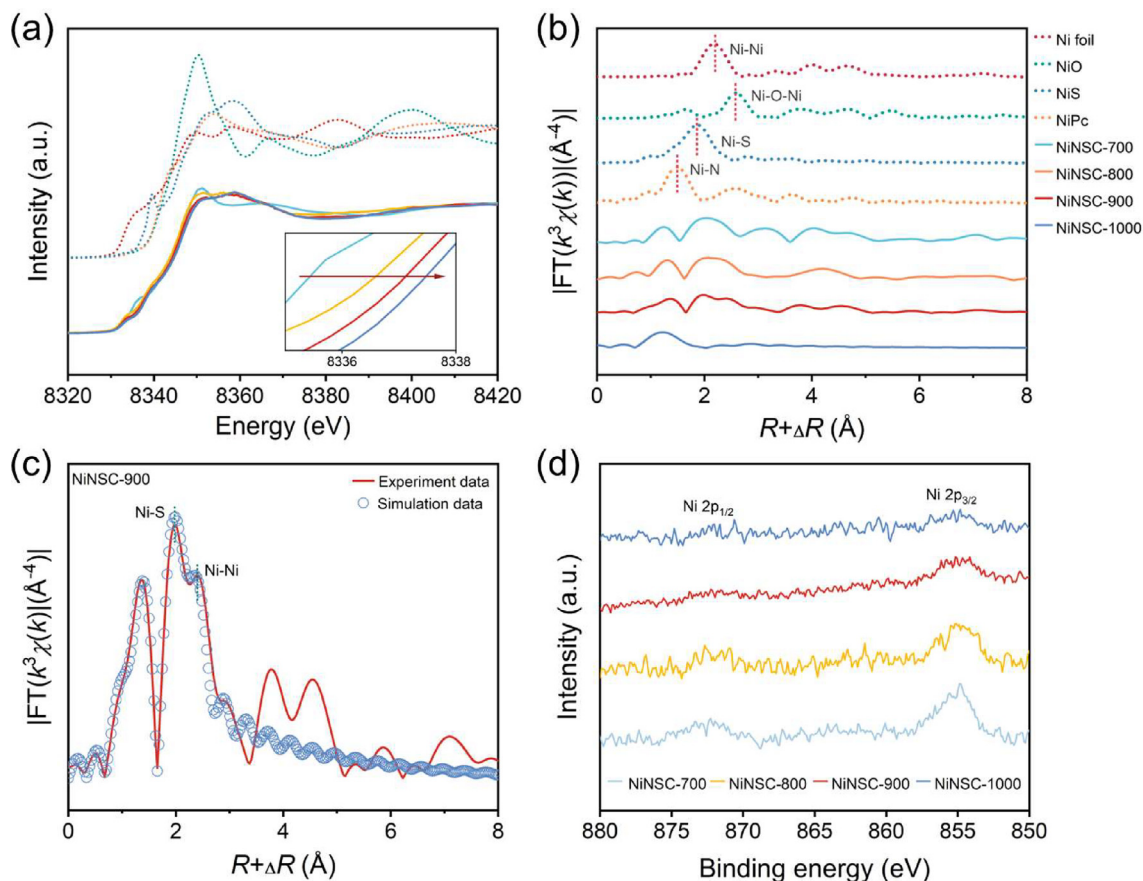


**Fig. 2.** (a) Ni K-edge XANES profiles and (b) EXAFS spectra of Ni foil, NiO, NiS, NiNSC-700, NiNSC-800, NiNSC-900 and NiNSC-1000. (c) Experiment data and fitted data of NiNSC-900 at R space. (d) High-resolution Ni 2p spectra of NiNSC-700, NiNSC-800, NiNSC-900, and NiNSC-1000.

of pyridinic N (398.08 eV), pyrrolic N (399.5 eV), graphitic N (400.4 eV), quaternary N (401.4 eV), and Ni–N (398.8 eV) species [37–39]. Notably, the Ni–N peak area diminishes from NiNSC-700 to NiNSC-1000, followed by the decrease of Ni contents. This confirms the formation of Ni–N sites and exclusion of the nanoparticles for NiNSC-700 to NiNSC-1000. The high-resolution S 2p spectra can be broken down to six peaks at 161.63, 163.71, 167.95, 162.68, 165.08 and 169.28 eV, separately attributed to the 2p<sub>3/2</sub> and 2p<sub>1/2</sub> of the S 2p (sulfide), S 2p (–C–S–C–) and S 2p (sulfate) [35,40]. For N, S Ni NPs, no obvious Ni–N bonds could be detected, and the high-resolution Ni 2p spectra displays different peaks from NiNSC-900. Extra satellite peaks of Ni 2p<sub>3/2</sub> (862.42 eV) and Ni 2p<sub>1/2</sub> (880.78 eV) indicate the existence of ordered crystal structure of Ni species as well (Fig. S18 online) [37].

The electrochemical CO<sub>2</sub>RR performance was initially evaluated in a classical three-electrode H-type cell system using 0.5 M KHCO<sub>3</sub> as the electrolyte. The LSV curves are presented in Fig. 3a. The current density of NiNSC-900 increases significantly when the electrolyte is changed from Ar-saturated to CO<sub>2</sub>-saturated, demonstrating its preference for the CO<sub>2</sub>RR process to the competitive hydrogen evolution reaction (HER) [20,23]. Moreover, NiNSC-900 achieves the lowest onset potential and highest current density under CO<sub>2</sub>-saturated conditions among the samples. Chronoamperometry measurements were performed from –0.3 to –0.9 V vs. RHE without *i*R compensation. The gas components were examined by an online GC system, and the liquid components were identified by offline <sup>1</sup>H NMR. NiNSC-900 exhibits the highest CO Faradaic efficiency (*FE*<sub>CO</sub>) of 98.75% at –0.6 V vs. RHE, which maintains above 95% over the whole applied potential range from –0.5 to –0.9 V vs. RHE (Fig. 3b). It also has the largest CO partial

current density (*j*<sub>CO</sub>) of –46.58 mA cm<sup>–2</sup> at –0.9 V vs. RHE (Fig. 3c), higher than NiNSC-800 (96.8%, –33.32 mA cm<sup>–2</sup>), NiNSC-700 (90.2%, –20.74 mA cm<sup>–2</sup>) and NiNSC-1000 (96.1%, –16.89 mA cm<sup>–2</sup>). However, N, S Ni NPs possesses negligible *j*<sub>CO</sub> (–0.46 mA cm<sup>–2</sup> at –0.9 V vs. RHE) and low *FE*<sub>CO</sub> (22.93% at –0.5 V vs. RHE), implying the ignorable catalytic activity of Ni nanoparticles toward CO production. Furthermore, NiNSC-900 delivers a lower Tafel slope of 87.64 mV dec<sup>–1</sup> than that of NiNSC-800 (101.99 mV dec<sup>–1</sup>), NiNSC-1000 (101.87 mV dec<sup>–1</sup>), NiNSC-700 (128.03 mV dec<sup>–1</sup>) and N, S Ni NPs (368.93 mV dec<sup>–1</sup>), indicating its faster reaction kinetics for CO<sub>2</sub>RR (Fig. S20a online) [41]. The Nyquist plots of all the catalysts were acquired from electrochemical impedance spectroscopy (EIS) measurements in H-cell. As shown in Fig. S20b (online), NiNSC-900 exhibits the lowest charge transfer resistance, which suggests faster electron transfer kinetics than the other contrast samples. On the contrary, the highest charge resistance was observed in N, S Ni NPs. Thus, the aggregation of Ni atoms into particles obstructs the rapid electron transfer and slows CO<sub>2</sub>RR kinetics [42]. The ECSAs are qualified by the double layer capacitances (*C*<sub>dl</sub>), which were acquired from electrochemical capacitance measurements (Fig. S19 online). NiNSC-900 gains higher *C*<sub>dl</sub> of 20.57 mF cm<sup>–2</sup> than those of NiNSC-800 (15.06 mF cm<sup>–2</sup>), NiNSC-700 (14.82 mF cm<sup>–2</sup>), NiNSC-1000 (12.61 mF cm<sup>–2</sup>), and N, S Ni NPs (11.83 mF cm<sup>–2</sup>), indicating a larger ECSA for NiNSC-900 owing to the abundant active sites and large surface areas [32]. Thus, the superiorities of NiNSC-900 in electrocatalytic CO<sub>2</sub>RR originate from abundant active sites, good conductivity, and larger surface areas. More importantly, the initial current density and high selectivity of NiNSC-900 with the *FE*<sub>CO</sub> of 95.26% was maintained after continuous electrolysis for 20 h in an

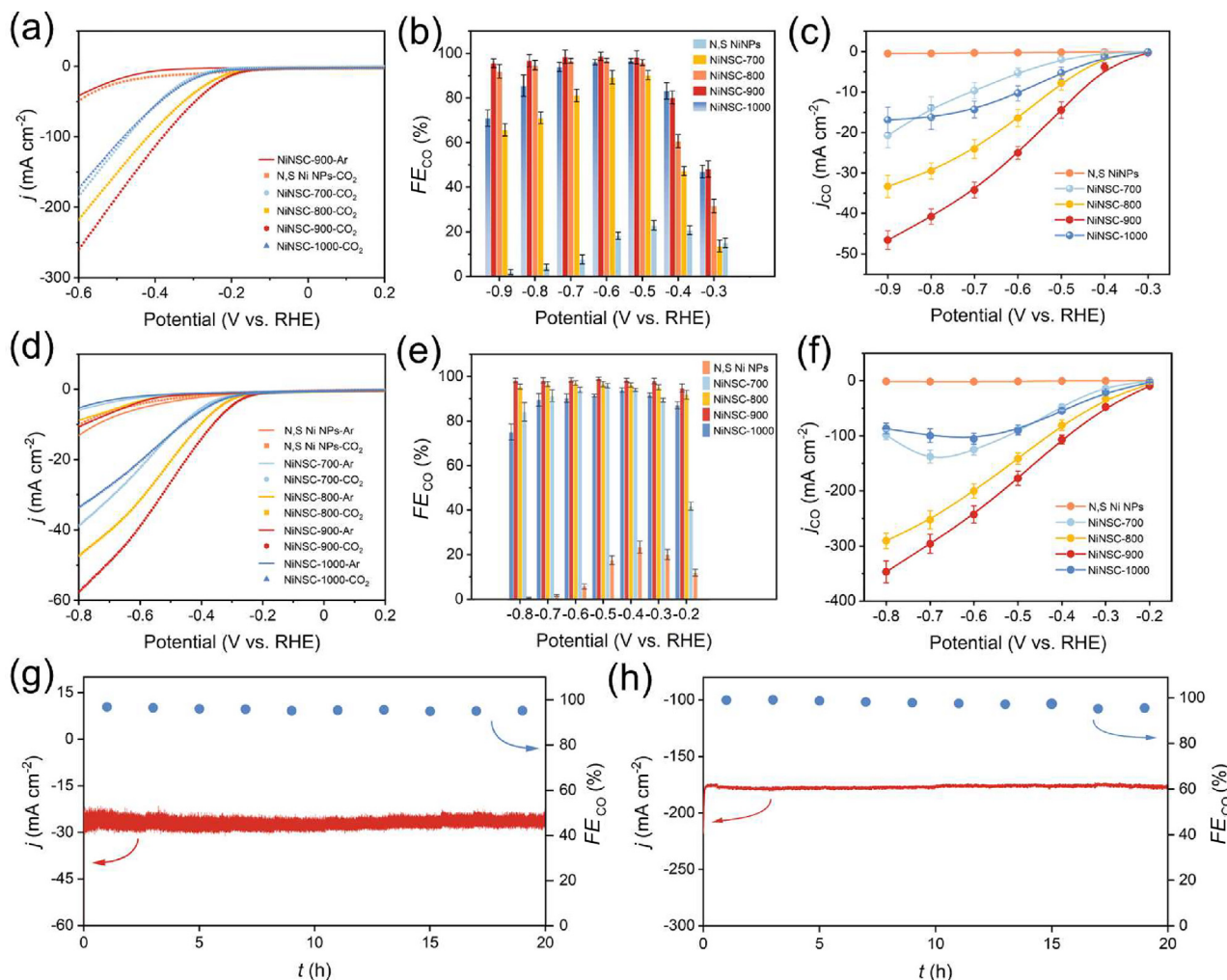


**Fig. 3.** (a, d) LSV curves of N, S Ni NPs, NiNSC-700, NiNSC-800, NiNSC-900, and NiNSC-1000 under CO<sub>2</sub> and Ar saturated electrolytes in H-cell (a) and flow cell (d). (b, e) FE<sub>CO</sub> for N, S Ni NPs, NiNSC-700, NiNSC-800, NiNSC-900 and NiNSC-1000 in H-cell (b) and flow cell (e). (c, f)  $j_{CO}$  for N, S Ni NPs, NiNSC-700, NiNSC-800, NiNSC-900 and NiNSC-1000 in H-cell (c) and flow cell (f). (g, h) Long-time durability of NiNSC-900 at  $-0.6$  V vs. RHE. in H-cell (g) and at  $-0.5$  V vs. RHE in a flow cell (h).

H-type cell (Fig. 2g). There was also no liquid product detected after the long CO<sub>2</sub>RR process (Fig. S21 online). No changes in the XRD pattern of NiNSC-900 were observed after 20 h electrolysis, as shown in Fig. S22a (online). This helps exclude the generation of Ni particles during the CO<sub>2</sub>RR process. The binding energies of N 1s, S 2p, and Ni 2p in the high-resolution N 1s, S 2p, and Ni 2p XPS spectra of NiNSC-900 after electrolysis (Fig. S22b–d online) possess negligible variation compared with primary NiNSC-900, therefore indicating the chemical structure of NiNSC-900 is highly stable. HAADF-STEM measurement was also carried out to identify the dispersion of Ni atoms after the lengthy electrolysis (Fig. S23 online). The slight corrosion on the surface of CNs after electrolysis could be attributed to the corrosive effect of KHCO<sub>3</sub> aqueous solution under applied potential, while the atomic dispersion of Ni sites can still maintain. Thus, the excellent stability of NiNSC-900 with multiple metal atom sites further highlights its promising future toward practical electrolysis CO<sub>2</sub>R to CO.

The feasibility of Ni FECC toward practical and industrial electrocatalytic CO<sub>2</sub>RR was further evaluated in a homemade flow cell system using 0.5 mol L<sup>-1</sup> KOH as the electrolyte. Here, the construction of a three-phase interface in the flow cell facilitates the suppression of the competing HER [43]. NiNSC-900 exhibits the lowest onset potential among the catalysts, which is also much lower than that gained in H-cell (Fig. 3d) due to the fast gas diffu-

sion. FE<sub>CO</sub> of NiNSC-900 remains more than 94% under different potentials ( $-0.3$  to  $-0.8$  V vs. RHE, Fig. 3e), with the optimal FE<sub>CO</sub> up to 99% at  $-0.5$  V vs. RHE. This is higher than NiNSC-700 (96%,  $-0.5$  V vs. RHE), NiNSC-800 (97%,  $-0.6$  V vs. RHE) and NiNSC-1000 (94%,  $-0.4$  V vs. RHE). Apart from the excellent selectivity, NiNSC-900 achieves an impressive  $j_{CO}$  of 347.2 mA cm<sup>-2</sup> at  $-0.8$  V vs. RHE, which greatly surpasses NiNSC-1000 (105.40 mA cm<sup>-2</sup>,  $-0.6$  V vs. RHE), NiNSC-700 (137.9 mA cm<sup>-2</sup>,  $-0.7$  V vs. RHE), and NiNSC-800 (290.6 mA cm<sup>-2</sup>,  $-0.8$  V vs. RHE) (Fig. 3f). Regarding the distinguished  $j_{CO}$  and FE<sub>CO</sub> of NiNSC-900, it thus supports the preponderance of dual and ternary Ni atoms sites over single-atoms and aggregating cluster sites in electrocatalytic CO<sub>2</sub>RR. More importantly, NiNSC-900 demonstrates satisfying and enduring durability in a flow cell with no apparent attenuation of the current density ( $\sim 178$  mA cm<sup>-2</sup>,  $-0.5$  V vs. RHE) under 20 h of unremitting electrolysis (Fig. 3h). The slight decrease of FE<sub>CO</sub> (from  $\sim 99\%$  to  $\sim 95.6\%$ ) results from the flooding of the gas diffusion electrode causing the formation and precipitation of the carbonates on the electrode. Moreover, NiNSC-900 also achieves excellent mass activity with 34,500 A g<sub>Ni</sub><sup>-1</sup> in H-cell and 128,600 A g<sub>Ni</sub><sup>-1</sup> in flow cell (Fig. S20c, d online). In summary, NiNSC-900 with multiple Ni atom catalytic sites also identified as a fully exposed cluster catalyst, is feasible in practical electrocatalytic CO<sub>2</sub>RR.

DFT calculations were implemented to understand the distinctive electrocatalytic performance of Ni FECC toward CO<sub>2</sub>RR. The calculated models were constructed according to the HAADF-STEM and XAFS results (Fig. S24 online). Attributing to the relatively weaker electronegativity of S than N, when a S atom replaces one of the N atoms in NiN<sub>4</sub>, less electrons from the central Ni atoms will be transfer to S/N atoms compared with that from Ni atom of NiN<sub>4</sub> to N atoms. This allows the formation of electron-rich centers and thus enhancing the adsorption of \*COOH intermediate on Ni site (Fig. 4a, b). As the number of Ni atoms and S atoms in the Ni clusters increases, the number of electrons around the Ni site increases. The corresponding Bader charges also exhibit a proportional relationship with the number of Ni/S atoms. These multi-atom sites with electron-rich centers further enhance the adsorption of \*COOH intermediates, resulting in a decrease of the corresponding energy barriers for forming \*COOH. Conversely, the desorption of \*CO gradually becomes progressively difficult upon increasing the doping number of S and Ni atoms in cluster sites. Therefore, suitable adsorption and desorption capacity of the intermediates on the active sites are necessary for accelerating the CO<sub>2</sub>-RR kinetics [44–46]. For example, the free energy for \*COOH formation on Ni<sub>3</sub>N<sub>3</sub>S<sub>3</sub> site is 0.07 eV, observably lower than that of the NiN<sub>4</sub> (1.81 eV), NiN<sub>3</sub>S (1.51 eV) and Ni<sub>2</sub>N<sub>4</sub>S<sub>2</sub> sites (0.73 eV). However, the Ni<sub>3</sub>N<sub>3</sub>S<sub>3</sub> site exhibits the highest free energy (1.66 eV) for \*CO desorption among the models. This suggests that the \*CO formed at the Ni<sub>3</sub>N<sub>3</sub>S<sub>3</sub> site is difficult to desorb, thus affecting the kinetics of the overall reaction [23]. Among the active sites, the Ni<sub>2</sub>N<sub>4</sub>S<sub>2</sub> site has moderate free energy levels available for \*COOH formation (0.73 eV) and \*CO desorption (1.0 eV). The comparison of the rate-determining step and corresponding energy barriers with other reported materials in the literature is shown in Table S5 (online), which indicates that the Ni<sub>2</sub>N<sub>4</sub>S<sub>2</sub> site possesses moderate reaction kinetics for CO<sub>2</sub>RR [47,48].

The differential charge density maps in Fig. 4c–f indicate that the electrons of Ni center will evenly transfer to the coordinated N atom in the case of the NiN<sub>4</sub> site. When S atoms were introduced, the electrons will be concentrated on the Ni–S bond and enhance the reactivity of these Ni sites [40]. In addition, multi-atom sites

exhibit stronger interactions with \*COOH intermediates than single-atom sites, which favor the adsorption of \*COOH and reduce the formation energy barrier of \*COOH. Therefore, the introduction of S atoms and the construction of multiple Ni atom active sites can rearrange the charge distribution around the active sites. Thus this enhances the interaction between catalytic sites and reactants, which is able to synergistically modulate the whole CO<sub>2</sub>RR kinetics.

#### 4. Conclusion

In summary, we have developed atomic-level dispersed Ni species, ranging from clusters to single-atoms, by manipulating the pyrolysis temperatures as efficient electrocatalysts for CO<sub>2</sub>RR to CO. Benefitting from the well-defined, fully exposed multiple-atom cluster sites and porous structure, the optimized Ni FECC achieves the maximal  $j_{CO}$  of 347.2 mA cm<sup>-2</sup>, a  $FE_{CO}$  exceeding 99%, as well as no apparent decay of the current density (~178 mA cm<sup>-2</sup>) after electrolysis for 20 h. DFT calculations reveal that the doped S atom plays a significant role in regulating the charge distribution of multiple Ni sites, allowing for optimized reaction kinetics in electrocatalytic CO<sub>2</sub> reduction to CO. This work highlights the significance of regulating the atomically dispersed metal atom catalysts in enhancing the electrocatalytic activity of transition metal-based catalysts, which can be expanded in other electrocatalytic processes.

#### Conflict of interest

The authors declare that they have no conflict of interest.

#### Acknowledgments

Hai-Xia Zhong acknowledges funding from the Alexander von Humboldt Foundation (Germany). This work was supported by the National Key R&D Program of China (2020YFB1505603), the National Natural Science Foundation of China (51925102), Key Research Program of the Chinese Academy of Sciences

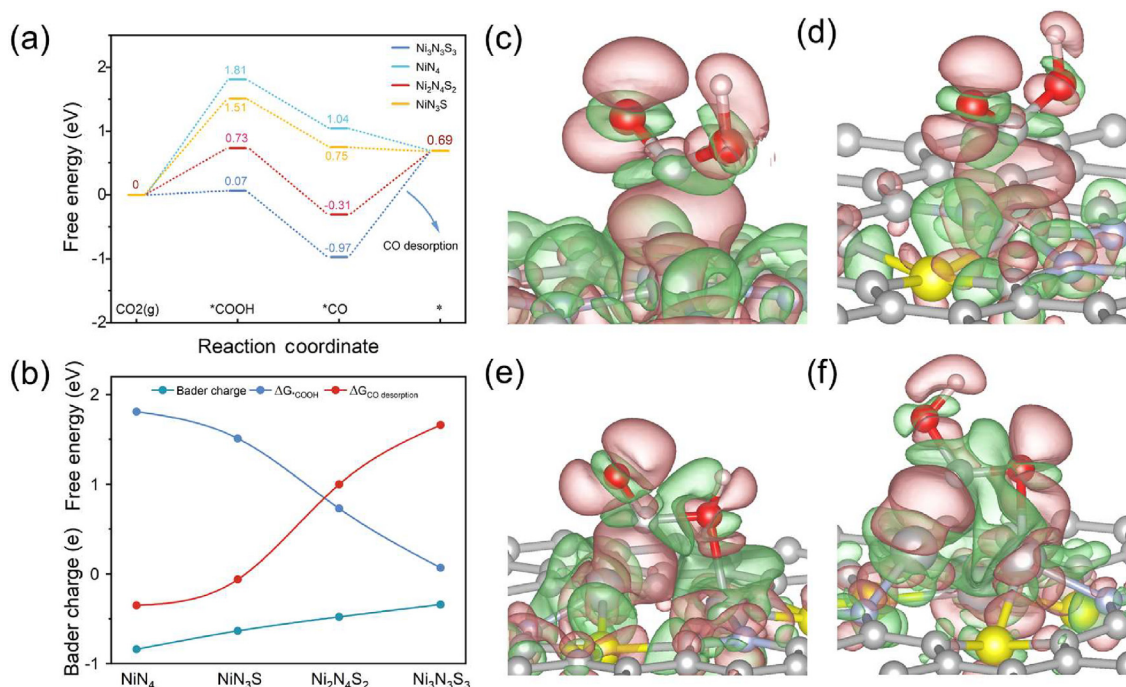


**Fig. 4.** (a) Free energy profiles of CO<sub>2</sub> electrocatalysis on NiN<sub>4</sub>, NiN<sub>3</sub>S, Ni<sub>2</sub>N<sub>4</sub>S<sub>2</sub> and Ni<sub>3</sub>N<sub>3</sub>S<sub>3</sub> sites. (b) Free energy of \*COOH and CO (g) in CO<sub>2</sub> electrocatalysis and Bader charge for NiN<sub>4</sub>, NiN<sub>3</sub>S, Ni<sub>2</sub>N<sub>4</sub>S<sub>2</sub>, and Ni<sub>3</sub>N<sub>3</sub>S<sub>3</sub>. (c–f) The differential charge density maps of the \*COOH intermediate on NiN<sub>4</sub> (c), NiN<sub>3</sub>S (d), Ni<sub>2</sub>N<sub>4</sub>S<sub>2</sub> (e), and Ni<sub>3</sub>N<sub>3</sub>S<sub>3</sub> (f) sites.

(ZDRW-CN-2021-3), and Youth Innovation Promotion Association CAS (E1202002).

### Author contributions

Xin-Bo Zhang conceived the idea and designed the experiments. Qi Hao and Qi Tang synthesized the materials and carried out the electrochemical testing. Qi Hao, Qi Tang, Hai-Xia Zhong and Dong-Xue Liu contributed to the characterizations and related discussions. Jia-Zhi Wang contributed to the theoretical calculations. Qi Hao, Qi Tang, Hai-Xia Zhong, Jia-Zhi Wang and Xin-Bo Zhang co-wrote the paper. All the authors discussed the results and commented on the manuscript. Qi Hao and Qi Tang contributed equally to this work.

### Appendix A. Supplementary materials

Supplementary materials to this article can be found online at <https://doi.org/10.1016/j.scib.2022.06.006>.

### References

- 1] Francke R, Schille B, Roemelt M. Homogeneously catalyzed electroreduction of carbon dioxide—methods, mechanisms, and catalysts. *Chem Rev* 2018;118:4631–701.
- 2] Qiao J, Liu Y, Hong F, et al. A review of catalysts for the electroreduction of carbon dioxide to produce low-carbon fuels. *Chem Soc Rev* 2014;43:631.
- 3] Birdja YY, Pérez-Gallent E, Figueiredo MC, et al. Advances and challenges in understanding the electrocatalytic conversion of carbon dioxide to fuels. *Nat Energy* 2019;4:732–45.
- 4] Chen C, Li Y, Yang P. Address the “alkalinity problem” in CO<sub>2</sub> electrolysis with catalyst design and translation. *Joule* 2021;5:737–42.
- 5] Aresta M, Dibenedetto A, Angelini A. Catalysis for the valorization of exhaust carbon: from CO<sub>2</sub> to chemicals, materials, and fuels. *Technological use of CO<sub>2</sub>*. *Chem Rev* 2014;114:1709–42.
- 6] Rogers C, Perkins WS, Veber G, et al. Synergistic enhancement of electrocatalytic CO<sub>2</sub> reduction with gold nanoparticles embedded in functional graphene nanoribbon composite electrodes. *J Am Chem Soc* 2017;139:4052–61.
- 7] Kim C, Jeon HS, Eom T, et al. Achieving selective and efficient electrocatalytic activity for CO<sub>2</sub> reduction using immobilized silver nanoparticles. *J Am Chem Soc* 2015;137:13844–50.
- 8] Ma M, Trześniewski BJ, Xie J, et al. Selective and efficient reduction of carbon dioxide to carbon monoxide on oxide-derived nanostructured silver electrocatalysts. *Angew Chem Int Ed* 2016;55:9748–52.
- 9] Zhu W, Zhang Y-J, Zhang H, et al. Active and selective conversion of CO<sub>2</sub> to CO on ultrathin Au nanowires. *J Am Chem Soc* 2014;136:16132–5.
- 10] Xiong Y, Sun W, Xin P, et al. Gram-scale synthesis of high-loading single-atomic-site Fe catalysts for effective epoxidation of styrene. *Adv Mater* 2020;32:2000896.
- 11] Xie X, He C, Li B, et al. Performance enhancement and degradation mechanism identification of a single-atom Co-N-C catalyst for proton exchange membrane fuel cells. *Nat Catal* 2020;3:1044–54.
- 12] Zhang L, Jia Y, Gao G, et al. Graphene defects trap atomic Ni species for hydrogen and oxygen evolution reactions. *Chem* 2018;4:285–97.
- 13] Li J, Chen S, Yang N, et al. Ultrahigh-loading zinc single-atom catalyst for highly efficient oxygen reduction in both acidic and alkaline media. *Angew Chem Int Ed* 2019;58:7035–9.
- 14] Zang W, Sun T, Yang T, et al. Efficient hydrogen evolution of oxidized Ni-N<sub>3</sub> defective sites for alkaline freshwater and seawater electrolysis. *Adv Mater* 2021;33:2003846.
- 15] Peng M, Dong C, Gao R, et al. Fully exposed cluster catalyst (FECC): toward rich surface sites and full atom utilization efficiency. *ACS Central Sci* 2021;7:262–73.
- 16] Zhang T, Han X, Yang H, et al. Atomically dispersed nickel(I) on an alloy-encapsulated nitrogen-doped carbon nanotube array for high-performance electrochemical CO<sub>2</sub> reduction reaction. *Angew Chem Int Ed* 2020;59:12055–61.
- 17] Ren W, Tan X, Yang W, et al. Isolated diatomic Ni-Fe metal-nitrogen sites for synergistic electroreduction of CO<sub>2</sub>. *Angew Chem Int Ed* 2019;58:6972–6.
- 18] Zhao G, Liu H, Ye J. Constructing and controlling of highly dispersed metallic sites for catalysis. *Nano Today* 2018;19:108–25.
- 19] Dong C, Li Y, Cheng D, et al. Supported metal clusters: fabrication and application in heterogeneous catalysis. *ACS Catal* 2020;10:11011–45.
- 20] Jiao J, Lin R, Liu S, et al. Copper atom-pair catalyst anchored on alloy nanowires for selective and efficient electrochemical reduction of CO<sub>2</sub>. *Nat Chem* 2019;11:222–8.
- 21] Su X, Jiang Z, Zhou J, et al. Complementary operando spectroscopy identification of *in-situ* generated metastable charge-asymmetry Cu<sub>2</sub>-CuN<sub>3</sub> clusters for CO<sub>2</sub> reduction to ethanol. *Nat Commun* 2022;13:1322.
- 22] Zhang M, Hu Z, Gu L, et al. Electrochemical conversion of CO<sub>2</sub> to syngas with a wide range of CO/H<sub>2</sub> ratio over Ni/Fe binary single-atom catalysts. *Nano Res* 2020;13:3206–11.
- 23] Fan Q, Hou P, Choi C, et al. Activation of Ni particles into single Ni-N atoms for efficient electrochemical reduction of CO<sub>2</sub>. *Adv Energy Mater* 2020;10:1903068.
- 24] Kresse G, Furthmüller J. Efficiency of *ab-initio* total energy calculations for metals and semiconductors using a plane-wave basis set. *Comp Mater Sci* 1996;6:15–50.
- 25] Blöchl PE. Projector augmented-wave method. *Phys Rev B* 1994;50:17953–79.
- 26] Perdew JP, Chevary JA, Vosko SH, et al. Atoms, molecules, solids, and surfaces: applications of the generalized gradient approximation for exchange and correlation. *Phys Rev B* 1992;46:6671–87.
- 27] Grimme S. Semiempirical hybrid density functional with perturbative second-order correlation. *J Chem Phys* 2006;124:034108.
- 28] Skúlason E, Bligaard T, Gudmundsdóttir S, et al. A theoretical evaluation of possible transition metal electro-catalysts for N<sub>2</sub> reduction. *Phys Chem Chem Phys* 2012;14:1235–45.
- 29] Zhao L, Zhang Y, Huang L-B, et al. Cascade anchoring strategy for general mass production of high-loading single-atomic metal-nitrogen catalysts. *Nat Commun* 2019;10:1278.
- 30] Rong X, Wang H-J, Lu X-L, et al. Controlled synthesis of a vacancy-defect single-atom catalyst for boosting CO<sub>2</sub> electroreduction. *Angew Chem Int Ed* 2020;59:1961–5.
- 31] Wu D, Wang X, Shi L, et al. Iron clusters boosted performance in electrocatalytic carbon dioxide conversion. *J Mater Chem A* 2020;8:21661–7.
- 32] Zhang E, Wang T, Yu K, et al. Bismuth single atoms resulting from transformation of metal-organic frameworks and their use as electrocatalysts for CO<sub>2</sub> reduction. *J Am Chem Soc* 2019;141:16569–73.
- 33] Xiong Y, Dong J, Huang Z-Q, et al. Single-atom Rh/N-doped carbon electrocatalyst for formic acid oxidation. *Nat Nanotechnol* 2020;15:390–7.
- 34] Ye W, Chen S, Lin Y, et al. Precisely tuning the number of Fe atoms in clusters on N-doped carbon toward acidic oxygen reduction reaction. *Chem* 2019;5:2865–78.
- 35] Hou Y, Qiu M, Kim MG, et al. Atomically dispersed nickel-nitrogen-sulfur species anchored on porous carbon nanosheets for efficient water oxidation. *Nat Commun* 2019;10:1392.
- 36] Wan X, Liu X, Li Y, et al. Fe-N-C electrocatalyst with dense active sites and efficient mass transport for high-performance proton exchange membrane fuel cells. *Nat Catal* 2019;2:259–68.
- 37] Zhu Z, Yin H, Wang Y, et al. Coexisting single-atomic Fe and Ni sites on hierarchically ordered porous carbon as a highly efficient ORR electrocatalyst. *Adv Mater* 2020;32:2004670.
- 38] Zhou H, Yang T, Kou Z, et al. Negative pressure pyrolysis induced highly accessible single sites dispersed on 3D graphene frameworks for enhanced oxygen reduction. *Angew Chem Int Ed* 2020;59:20465–9.
- 39] Yang Q, Yang C-C, Lin C-H, et al. Metal-organic-framework-derived hollow N-doped porous carbon with ultrahigh concentrations of single Zn atoms for efficient carbon dioxide conversion. *Angew Chem Int Ed* 2019;58:3511–5.
- 40] Zhou H, Zhao Y, Gan J, et al. Cation-exchange induced precise regulation of single copper site triggers room-temperature oxidation of benzene. *J Am Chem Soc* 2020;142:12643–50.
- 41] Zhang Z, Feng C, Liu C, et al. Electrochemical deposition as a universal route for fabricating single-atom catalysts. *Nat Commun* 2020;11:1215.
- 42] Wu Q, Liang J, Xie Z-L, et al. Spatial sites separation strategy to fabricate atomically isolated nickel catalysts for efficient CO<sub>2</sub> electroreduction. *ACS Mater Lett* 2021;3:454–61.
- 43] Endrődi B, Samu A, Kecsenovity E, et al. Operando cathode activation with alkali metal cations for high current density operation of water-fed zero-gap carbon dioxide electrolyzers. *Nat Energy* 2021;6:439–48.
- 44] Lin L, Li H, Yan C, et al. Synergistic catalysis over iron-nitrogen sites anchored with cobalt phthalocyanine for efficient CO<sub>2</sub> electroreduction. *Adv Mater* 2019;31:1903470.
- 45] Yan C, Li H, Ye Y, et al. Coordinatively unsaturated nickel-nitrogen sites towards selective and high-rate CO<sub>2</sub> electroreduction. *Energy Environ Sci* 2018;11:1204–10.
- 46] Jia C, Tan X, Zhao Y, et al. Sulfur-dopant-promoted electroreduction of CO<sub>2</sub> over coordinatively unsaturated Ni-N<sub>2</sub> moieties. *Angew Chem Int Ed* 2021;60:23342–8.
- 47] Ren W, Tan X, Jia C, et al. Electronic regulation of Ni single atom by confined Ni nanoparticles for energy-efficient CO<sub>2</sub> electroreduction. *Angew Chem Int Ed* 2022:e202203335.
- 48] Zhu W, Zhang L, Liu S, et al. Enhanced CO<sub>2</sub> electroreduction on neighboring Zn/Co monomers by electronic effect. *Angew Chem Int Ed* 2020;59:12664–8.



Qi Hao is currently a M.S. candidate at Key Laboratory of Automobile Materials, Ministry of Education, Jilin University. He received his B.S. degree at Anhui University in 2018. His research interest focuses on electrochemical carbon dioxide reduction reaction.



Xin-Bo Zhang is a Professor at State Key Laboratory of Rare Earth Resource Utilization, Changchun Institute of Applied Chemistry, Chinese Academy of Sciences. The ongoing researches in Zhang's group includes rechargeable batteries and electrocatalysis.



Qi Tang received her B.S. degree at Jilin University in 2020. Now she is a Ph.D candidate under the guidance of Prof. Xin-Bo Zhang at State Key Laboratory of Rare Earth Resource Utilization, Changchun Institute of Applied Chemistry, Chinese Academy of Sciences. Her research interest focuses on electrocatalytic reduction reaction of carbon dioxide.